



Direct Observations of Precursor Short-Range Order Clusters of Solute Atoms in a LPSO-Forming Mg-Zn-Gd Ternary Alloy

D. Egusa¹, K. Kawaguchi¹ and E. Abe^{1,2*}

¹ Department of Materials Science and Engineering, University of Tokyo, Tokyo, Japan, ² Research Center for Structural Materials, National Institute for Materials Science, Tsukuba, Japan

OPEN ACCESS

Edited by:

Hajo Dieringa,
Helmholtz Centre for Materials and
Coastal Research (HZG), Germany

Reviewed by:

Chamini Mendis,
Brunel University London,
United Kingdom
Mingyi Zheng,
Harbin Institute of Technology, China

*Correspondence:

E. Abe
abe@material.t.u-tokyo.ac.jp

Specialty section:

This article was submitted to
Structural Materials,
a section of the journal
Frontiers in Materials

Received: 13 August 2019

Accepted: 14 October 2019

Published: 30 October 2019

Citation:

Egusa D, Kawaguchi K and Abe E
(2019) Direct Observations of
Precursor Short-Range Order Clusters
of Solute Atoms in a LPSO-Forming
Mg-Zn-Gd Ternary Alloy.
Front. Mater. 6:266.
doi: 10.3389/fmats.2019.00266

We have investigated short-range order (SRO) clusters of solute atoms in a Mg₉₇Zn₁Gd₂ alloy which forms a long-period stacking/order (LPSO) phase, based on aberration-corrected scanning transmission electron microscopy (STEM) observations and first-principles calculations. High-angle annular dark-field (HAADF) STEM provides directly the individual Gd atom positions through significant atomic-number dependent Z-contrast, and their averaged image-processing have immediately shown up the representative SRO-Gd configurations being in favor of the second-nearest networks in the *hcp*-Mg structure. Interestingly, Zn atoms seem to be essentially placed at the particular sites within the SRO-Gd configurations to form D0₁₉-like ZnGd₃ clusters, a validity of which are verified by STEM image simulations and first-principles calculations. These D0₁₉-like ZnGd₃ clusters in the *hcp*-Mg matrix are likely to be a precursor sub-structure to the L1₂-type Zn₆Gd₈ clusters that are embedded in the local *fcc* layers in the LPSO structure. In fact, we find that these D0₁₉-like ZnGd₃ clusters seem to form a layered atmosphere prior to the LPSO formation, providing an important clue on how the LPSO phases nucleate and grow.

Keywords: Mg alloys, long-period stacking/order (LPSO) phase, solute clusters, scanning transmission electron microscopy, first-principles calculations

INTRODUCTION

Since Mg has the lowest density among practical metals, it is expected to use for transportation equipment such as aircraft and automobiles for improving their energy efficiency (Egami et al., under review). Owing to a low strength and a poor ductility of Mg, it is practically alloyed with a trace amount of additive elements. Rare earth elements (hereinafter denoted as RE) have been known as one of the effective alloying elements that significantly improve the mechanical properties of Mg alloys (Homma et al., 2009; Nie, 2012; Sandlöbes et al., 2014), which are originated from such as the texture weakening by solute segregations or the age hardening due to fine precipitations of the Mg-RE compounds. However, adding a large amount of RE impairs the lightness of Mg alloys, so many studies have been conducted on alloy designs with a limited amount of RE additions.

In recent years, Mg alloys with a small addition of RE and transition metals (TM) have attracted wide attentions because they exhibit excellent mechanical properties (Kawamura et al., 2001; Itoi et al., 2004; Yamasaki et al., 2005; Honma et al., 2007; Kawamura and Yamasaki, 2007; Hagihara et al., 2010). In these ternary alloys, various kinds of precipitates form depending on the additive

elements and the heat-treatment conditions (Honma et al., 2005; Matsushita et al., 2016; Fujita et al., 2018; Gu et al., 2018; Koizumi et al., 2018). In particular, Mg-Zn-RE ternary alloys have been focused as one of the candidates for next-generation lightweight alloys, which indeed show excellent mechanical properties due to the presence of the long period stacking/order (LPSO) phase (Abe et al., 2002, 2011; Kawamura and Yamasaki, 2007; Zhu et al., 2010; Egusa and Abe, 2012; Kim and Kawamura, 2013; Saal and Wolverton, 2014; Egami and Abe, 2015; Yamashita et al., 2019) as a strengthening phase via kink deformation (Kawamura and Yamasaki, 2007; Homma et al., 2009; Shao et al., 2010; Egusa et al., 2013; Yamasaki et al., 2013; Xu et al., 2015; Garcés et al., 2018; Hagihara et al., 2019; Inamura, 2019). The LPSO structures consist of stacking order as well as chemical order with respect to the hexagonal close-packed (*hcp*) Mg structure. A distinctive structural-unit represented by Intrinsic-II type stacking faults (I_2 -SF) forms a local face-centered cubic (*fcc*) stacking environment, in which the additive Zn/RE elements are commonly distributed (Abe et al., 2002, 2011). The solute-enriched I_2 -SF (SESF: solute-enriched stacking fault) is a basic-unit of the LPSO phases, and the isolated SESFs can be distributed randomly in the *hcp*-Mg matrix (Yamasaki et al., 2007; Nie et al., 2008; Egami et al., under review). In addition, further analysis on the LPSO structure showed that Zn and RE are ordered to form the $L1_2$ -type cluster embedded within the *fcc*-SESF (Yokobayashi et al., 2011; Egusa and Abe, 2012; Ma et al., 2013; Saal and Wolverton, 2014; Okuda et al., 2015; Hosokawa et al., 2018; Nishioka et al., 2018), which indeed plays an important role for increasing thermodynamic stability of the SESF (Egami et al., under review).

It is known that these Mg-Zn-RE systems are classified into Type I (RE = Y, Dy, Ho, Er, Tm) and Type II (RE = Gd, Tb) according to formation of the LPSO phase during solidifications or aging processes (Kawamura and Yamasaki, 2007). Mg-Zn-Gd alloys, classified into Type II, precipitate the LPSO phase during an isothermal annealing, whose behaviors were experimentally summarized as a time-temperature-transformation (TTT) diagram (Yamasaki et al., 2007). Solute-enriched platelet zones (Guinier-Preston like zone) are formed at relatively low temperatures ($< \sim 500$ K) (Nishijima et al., 2008; Saito et al., 2011; Koizumi et al., 2018). On the other hand, the LPSO phase and SESFs are formed in the α -Mg matrix at relatively high temperature (Jono et al., 2013; Gröbner et al., 2015). It should be noted here that Zn is essential for the formation of these various precipitates/zones, which have never been available for the Mg-Gd binary alloys (He et al., 2006; Nishijima and Hiraga, 2007).

Clustering of solute elements and the introduction of the I_2 -SF are essential events for formation of the LPSO structure. Recent studies have suggested two possible formation processes of the LPSO structures; one driven by the introduction of the I_2 -SF, and the other driven by spinodal-like phase separation which involves clustering of solute atoms (Yamamoto et al., 2013; Umebayashi et al., 2014; Okuda et al., 2015, 2017; Egami et al., under review). Okuda et al. investigated precipitation processes of the LPSO phase from the amorphous Mg-Zn-RE alloys in the quenched ribbon sample by *in-situ* synchrotron X-ray observations (Okuda et al., 2017). They reported that there is a short-range order

(SRO) of solute element at the initial stage of the LPSO phase formation, whose sizes are corresponding to about a solute dimer in the amorphous state, and they grow in the crystalline *hcp*-Mg state. Photoemission spectroscopy investigations also supported formation of the solute SRO clusters at the initial stage of the LPSO phase formation, suggesting that the SRO is a precursor phenomenon to form the $L1_2$ -type clusters (Hosokawa et al., 2018). Such precursor phenomenon significantly affects on the thermodynamics of the LPSO phase formation; however, the detailed structures and spatial distributions of such SRO clusters are not clarified yet. In the present study, we investigate the precursor SRO clusters in the *hcp*-matrix of a Mg-Zn-Gd alloy based on direct observations using advanced electron microscopy, and discuss their detailed structures and spatial distributions in terms of the LPSO phase formation.

MATERIALS AND METHODS

A nominal composition of the alloy used in the present study was $Mg_{97}Zn_1Gd_2$ (at. %). Master alloy ingots were prepared by high frequency induction melting of pure metals in an argon atmosphere. In order to control ordering and distributions of the SESF, the alloy ingots were solution treated at 793 K for 2 h, followed by water quench, and then annealed at 573 K for 10 h (Yamasaki et al., 2007). All the heat treatments were performed using a Pyrex tube in an argon atmosphere after evacuation to pressures lower than 3×10^{-3} Pa. Microstructures of the samples were observed by scanning electron microscopy (SEM, JEM-7900F) using backscattering electron (BSE) detector at the accelerating voltage of 15 kV. For atomic-resolution high-angle annular dark-field (HAADF)-scanning transmission electron microscopy (STEM) observations, we used an aberration-corrected 200 kV STEM (JEM-ARM200F) that provides a minimum probe of ~ 0.8 Å with a convergence semi-angle of 22 mrad. For HAADF imaging, the annular detector was set to collect the electrons scattered at angles higher than 90 mrad, which is sufficiently high to reveal a chemical sensitive Z-contrast. Thin foils for STEM observations were prepared by standard Ar-ion milling. Image simulations were carried out using the xHREM software based on the fast-Fourier-transform multi-slice algorithm (Ishizuka, 2002). First-principles calculations were performed to evaluate formation energies of the *hcp*-Mg crystals containing solute atoms. The super cell size for calculations was $5 \times 5 \times 4$ with respect to the primitive *hcp*-Mg structure, containing 200 atoms. Structural optimizations were performed by using the Vienna Ab initio Simulation Package (VASP) code within the framework of density-functional theory (Kresse and Furthmüller, 1996), based on generalized gradient approximation (Perdew et al., 1992), and ultrasoft scalar relativistic pseudo-potentials (detailed conditions for calculations are described in the **Figure 4** captions).

RESULTS

Figure 1a shows a SEM-BSE image obtained from a heat-treated $Mg_{97}Zn_1Gd_2$ alloy. Bright-contrast regions in the image

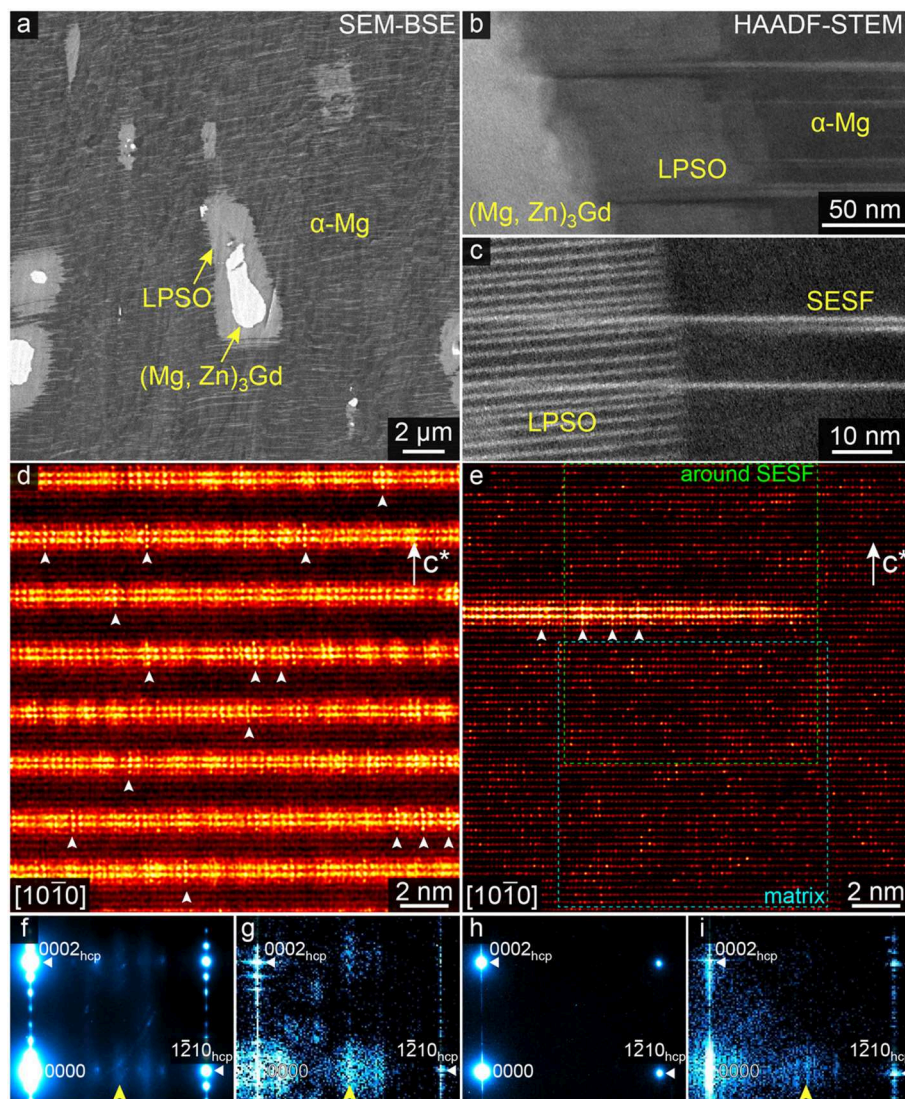
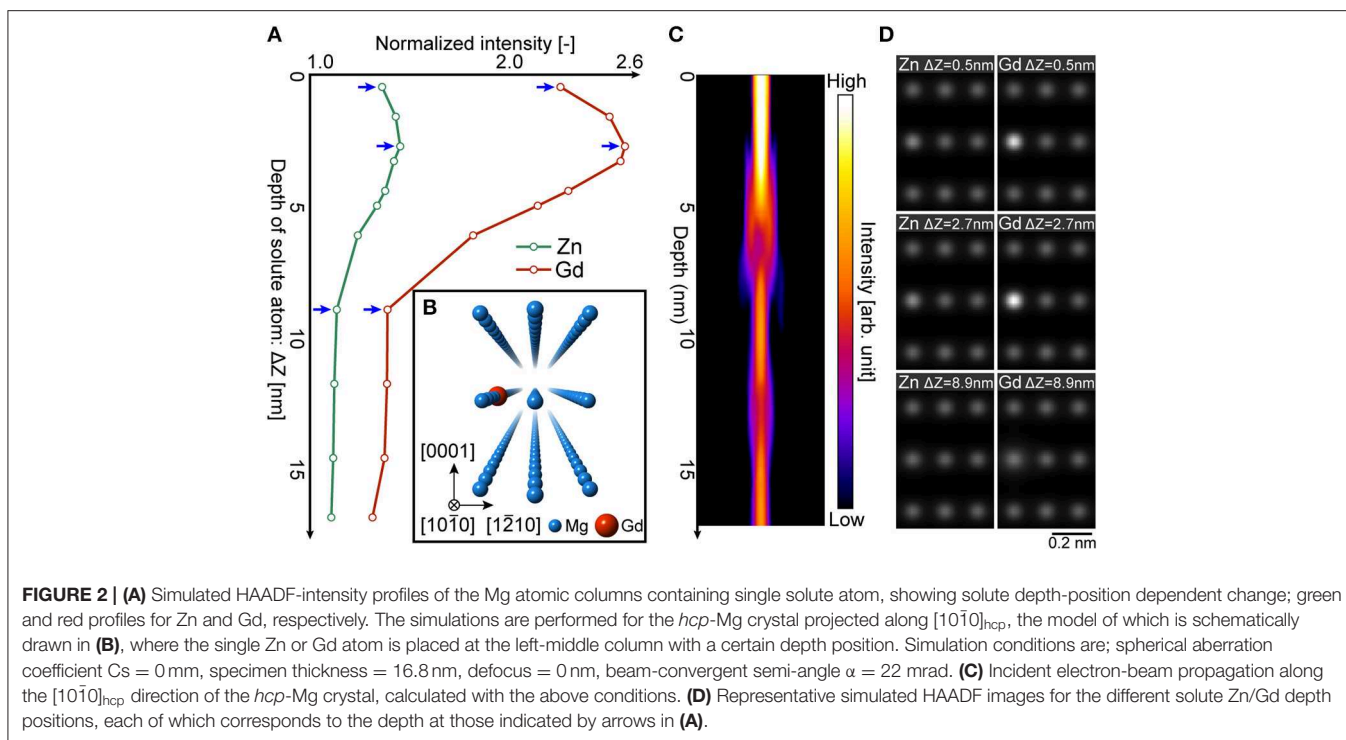


FIGURE 1 | (a) SEM-BSE image taken from a heat-treated $\text{Mg}_{97}\text{Zn}_1\text{Gd}_2$ alloy. (b,c) HAADF-STEM images of the multiple-phase coexisting regions of the $(\text{Mg,Zn})_3\text{Gd}$ compound, the LPSO phase and the $\alpha\text{-Mg}$ phase with essential SESFs. (d,e) Atomic-resolution HAADF-STEM images of the 14H-type LPSO phase and the $\alpha\text{-Mg}$ matrix along the $[10\bar{1}0]_{\text{hcp}}$ directions, respectively. c^* denotes the c -axis of the matrix crystals. Blue and green dotted rectangles in (e) correspond to the enlarged areas shown in Figures 3a, 7a, respectively. (f) EDP and (g) PS calculated from the LPSO phase images of (d), and (h,i) represent those for the $\alpha\text{-Mg}$ matrix image of (e) in the same manner, respectively. The indices of the major reflections in EDPs and PSs are given based on the hcp -Mg structure.

correspond to the $(\text{Mg,Zn})_3\text{Gd}$ compound and the LPSO phase, as denoted in the image. The $(\text{Mg,Zn})_3\text{Gd}$ compound does not fully dissolve and remains even after the solution-treatment (Jono et al., 2013). The $(\text{Mg,Zn})_3\text{Gd}$ compounds are surrounded by the LPSO phases, suggesting that the LPSO phase has formed from the Zn/Gd-rich compound during the heat-treatment. In addition, a large number of thin bright lines in the $\alpha\text{-Mg}$ matrix can be seen clearly, which correspond to the SESF and/or very fine platelet LPSO precipitates. Figure 1b shows a HAADF-STEM image obtained around the $(\text{Mg,Zn})_3\text{Gd}$ compound and the LPSO phase. The LPSO phase is continuously formed from the $(\text{Mg,Zn})_3\text{Gd}$ compound, and the SESFs are grown from the

edge of the LPSO phase, as clearly seen in Figure 1c. We below investigate details of solute arrangements in the $\alpha\text{-Mg}$ matrix.

Figures 1d,e show HAADF-STEM images of the 14H-type LPSO phase and the $\alpha\text{-Mg}$ matrix, taken along the $[10\bar{1}0]_{\text{hcp}}$ directions. The corresponding electron diffraction patterns (EDP) and the power spectra (PS) of the images of Figures 1d,e are shown in Figures 1f–i, respectively. HAADF imaging provides a significant atomic-number dependent contrast, so that bright dots in the images represent the Zn and/or Gd enriched atomic columns. White arrowheads in the LPSO structure image of Figure 1d indicate characteristic bright-dot configurations representing the $\text{L}1_2$ -type Zn_6Gd_8 clusters, which are successfully

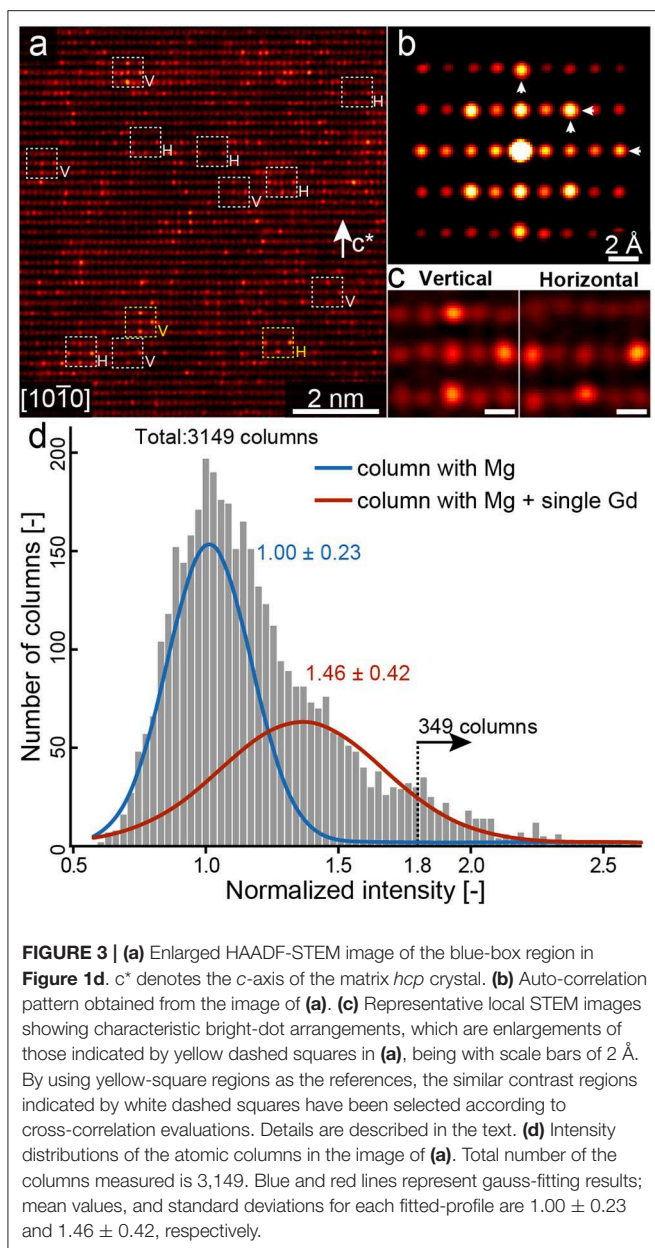


imaged in the $[10\bar{1}0]_{\text{hcp}}$ projection. The $L1_2$ - Zn_6Gd_8 clusters can be arrayed in an ordered manner within the SESF (i.e., in-plane order) due to inter-cluster interactions (Kimizuka et al., 2014; Yamasaki et al., 2014; Yamashita et al., 2019). For the present LPSO phase, the number of weak peaks between 0000 and $1\bar{2}10$ reflections in the EDP (Figure 1f) indicates $6 \times (1\bar{2}10)$ order in average. In addition, note that weak diffuse peak appears in the corresponding PS (Figure 1g) as indicated by the arrowhead, representing the Zn/Gd SRO due to presence of the $L1_2$ -type clusters. The diffuse peak is not obvious in the EDP but significantly enhanced in the PS, since the latter has been reconstructed from the HAADF image whose information is highly weighted to heavy-atom configurations (i.e., highly sensitive to the SRO structures composed of heavy atoms).

By looking the image of Figure 1e, there also appears the characteristic $L1_2$ -type SRO contrast within the SESF such as indicated by arrowheads, suggesting the $L1_2$ -type cluster formation even in the isolated SESF (Egami et al., under review). Note that there are no significant peaks between 0000 and $1\bar{2}10$ in the DP (Figure 1h), but there indeed appears a diffuse peak in the PS (Figure 1i), as indicated by the arrowhead. This is again due to a significant atomic-number weighted Z-contrast of the HAADF imaging, which is able to enhance largely the hidden heavy-atom structures if any. Therefore, the solute SRO cluster formation can be highly anticipated within the α -Mg matrix, details of which will be discussed later.

In order to clarify the solute SRO structures, we first attempt simulations on how the single Zn/Gd atoms in the α -Mg matrix are imaged by an aberration-corrected HAADF-STEM. Figure 2A shows simulated HAADF-intensity profiles constructed by varying a depth position of the single solute atom

in the atomic column, as schematically drawn in Figure 2B. Simulations are performed for the *hcp*-Mg crystal projected along the $[10\bar{1}0]_{\text{hcp}}$, and the specimen thickness is set to be 16.8 nm based on electron-energy-loss spectroscopy (EELS) log-ratio measurements (Malis et al., 1988). The image intensity is normalized with respect to that of the pure Mg atomic column. Both for the Zn and Gd atoms, the intensity profiles show the highest values when the solute atom is located at the depth of 2.7 nm from the surface, and the intensity becomes almost constant when the solute atoms are located beyond the depth of 8.9 nm. Figure 2C shows the focused electron-beam channeling behaviors propagated along the $[10\bar{1}0]_{\text{hcp}}$ direction in the *hcp*-Mg crystal. Due to dynamical diffraction effects with a wide convergence angle of the modern aberration-corrected STEM, the beam intensity exhibits a certain maximum at a few nanometers below the surface and oscillates along the propagating direction (Mittal and Mkhoyan, 2011). By comparing the intensity profiles (Figure 2A) and the beam propagations (Figure 2C), it immediately turns out that the column intensities show their maxima when the solute atoms are placed at the depth position relevant to the beam-flux maximum. Therefore, the column-intensity variations in the *hcp*-Mg matrix (e.g., see Figure 1d) are governed by the individual solute atoms placed at a certain depth range. Figure 2D shows the representative simulated images with the solute atoms placed at 0.5, 2.7, and 8.9 nm in depth positions, respectively, which correspond to those indicated by blue arrows in Figure 2A. Again, the column intensities are sufficiently strong when the solute atoms are located at the depth near the surface, and become hardly distinguishable when the solute atoms are at the deeper positions. Since the composition of the present



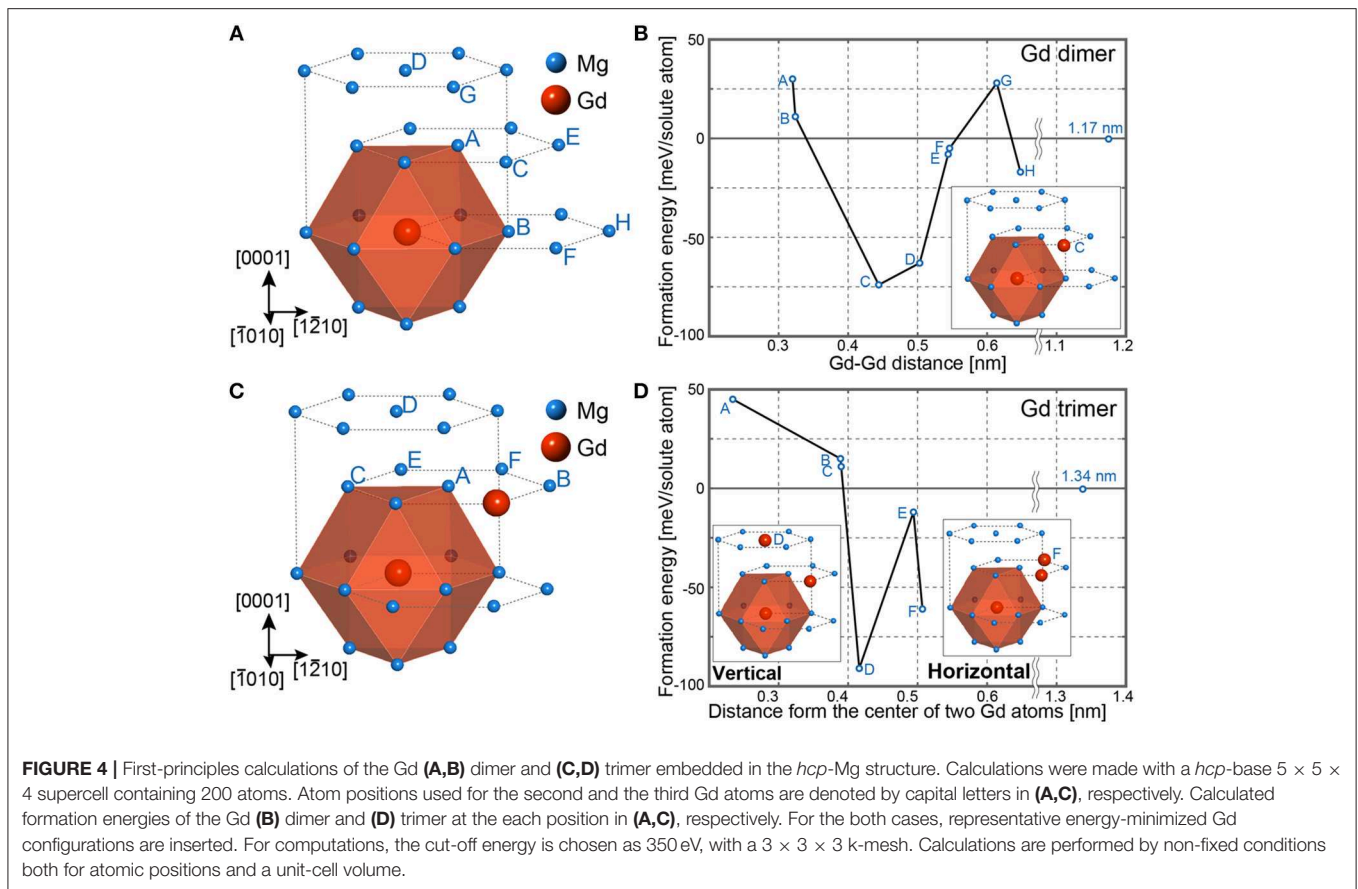
hcp -Mg matrix is sufficiently dilute (Mg-0.3at.%Zn-0.8at.%Gd by SEM-EDS analysis), we assume that there is almost no plurality of solute atoms in the same atomic column for a thin specimen (~ 17.0 nm for the present case), leading that the column intensities higher than 1.8 are likely to represent the single Gd atoms in the hcp -Mg matrix (i.e., individual single Gd atoms placed at the depth up to 6.1 nm are detected in the experiment).

Figure 3a shows a HAADF-STEM image obtained from the α -Mg matrix at the position indicated by the dotted blue-rectangle in Figure 1e. Intensity variations at each of the columns in the image directly represent the distribution of individual solute atoms, as governed mostly by Gd atoms. Figure 3b shows an auto-correlation pattern constructed from Figure 3a, reflecting

the spatial correlation of the bright dots in the STEM image. The strong spots indicated by white arrowheads suggest directly the SRO correlations by the solute atoms, corresponding to the second- and/or third-nearest neighbor atomic sites projected along $[1\bar{2}10]$ direction. Note that there are some characteristic configurations of the bright dots, such as indicated by the dotted rectangles in Figure 3a (see the figure caption for the yellow/white representations). Figure 3c exemplifies the two typical configurations, denoted as “vertical” and “horizontal,” whose details will be discussed later. In order to evaluate the column-intensity distributions, we have extracted the intensity of the individual atomic columns and applied gaussian fitting. Figure 3d shows the intensity distribution measured from 3,149 atomic columns in the α -Mg matrix image. As demonstrated in Figure 2A, the normalized intensity of the Zn-containing column appears about 1.2 at the highest, suggesting that Zn distributions can hardly be distinguished solely by HAADF intensity. Therefore, the intensity distributions are supposed to be two groups, i.e., the most columns are with pure Mg and containing single Gd atom. The red and blue profiles in Figure 3d correspond to the gaussian-fitted results of the column intensity distributions, respectively. Based on the fitted result with the reasonably high R-square value of 0.987, the average intensity of the columns containing single Gd atom is estimated as 1.46 with respect to the pure Mg columns, the value of which fairly matches to the image simulations (Figure 2). According to the above analysis, the number of columns with the intensity higher than 1.8 turns out to be 349, which is about 11% for the total number of the measured atomic columns (3,149). The intensity level of 1.8 is relevant to the single Gd atom located up to the depth of 6.1 nm from the surface; i.e., single Gd atom per 10 Mg atoms can be roughly estimated based on the hcp -Mg crystal in the $[10\bar{1}0]_{hcp}$ projection (see Figure 2). Therefore, the solute Gd fraction in the α -Mg matrix is derived as being about 1.1at.% (11%/10), which is not largely deviated from the estimated matrix composition (0.8at.%Gd by SEM-EDS analysis) and hence support the validity of imaging individual Gd atoms.

DISCUSSION

Presence of the SRO clusters is directly indicated by STEM observations, as shown in Figure 3c. Here, we investigate possible SRO structures by comparing formation energies of various Gd atom arrangements using first-principles calculations. Figure 4A shows a model for placing two Gd atoms in the hcp -Mg structure. Position of the first Gd atom is fixed at the center of the polyhedron represented by orange planes, and the second Gd atom is placed at the positions denoted by capital letters from A to H. Figure 4B shows the calculated formation energies for the two Gd atom configurations. Energy base-line is set to the one calculated when the Gd atoms are sufficiently separated (apart more than 1 nm) and hence their interactions can be sufficiently negligible. The lowest formation energy is obtained when the second Gd atom is placed at the C site, whose configuration is inserted in Figure 4B. Two Gd and four Mg are located at the octahedral sites, and the Gd-Gd configuration corresponds to the

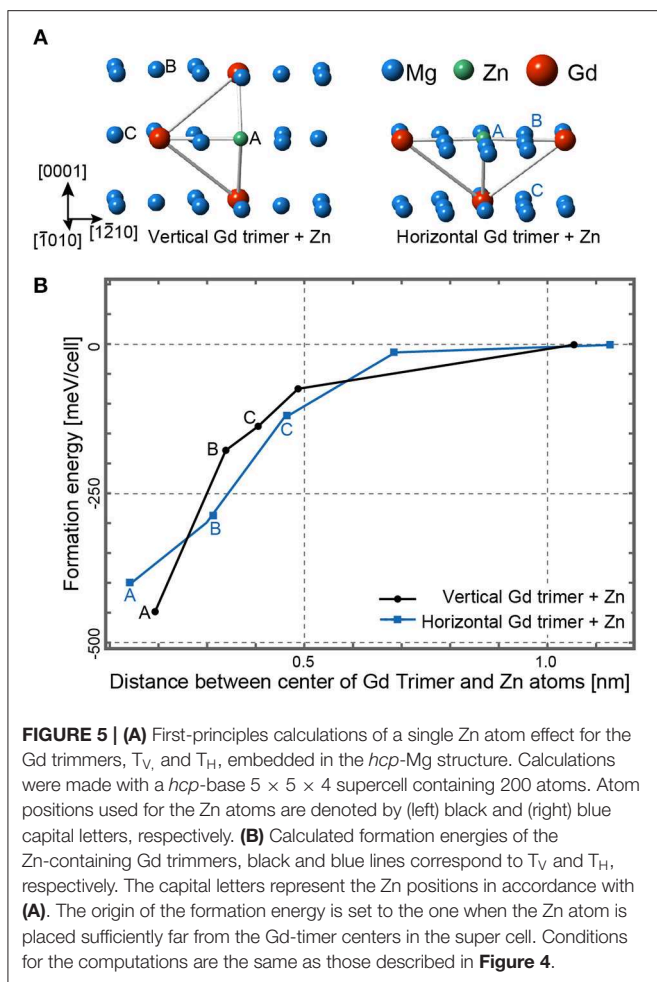


second-nearest neighbor in the *hcp*-Mg structure. Note that the second-nearest neighbor RE arrangements represents a partial structure of a $D0_{19}$ -type order, which is commonly observed in various Mg-RE compounds (Nie, 2012). We termed the pair of these Gd configurations as “dimer” hereafter. In fact, dimer RE configurations appear to be frequent in the observed STEM image (Figure 3); though, further extended SRO configurations, such as indicated in Figure 3c, turn out to be also prominent in the present alloy.

Figure 4C shows a model for placing triple Gd atoms in the *hcp*-Mg structure, in which two Gd atoms are already fixed at the stable dimer environments, and the third Gd is placed at the positions denoted from A to F. Figure 4D shows calculated formation energies of the models. The energy-base is also set when the Gd atoms are sufficiently separated (more than 1 nm) in the super cell. There are two positions that give local minima for the formation energy, D and F, whose Gd arrangements are inserted in Figure 4D. We termed these Gd configurations as “vertical trimer (T_V)” and “horizontal trimer (T_H)” for the models with the third Gd atom at the D and F sites, respectively (note that the “D” site already appears as an energetically favorable position during dimer considerations; namely, the simultaneous Gd atoms both at the C and D sites in Figure 4B provide the T_V configuration). For the both trimers, the third Gd atom to the dimer is placed at the second-nearest neighbor to the other Gd atoms. It should be noted here that

the Gd configurations in T_V and T_H are relevant to the bright-dot arrangements those frequently observed in Figure 3a, as indicated by dashed squares denoted with V and H, respectively. Also, the bright-dot appearances in the auto-correlation pattern (Figure 3b) can be explained by these two types of the Gd trimer, T_V and T_H , supporting that these trimer configurations are representative solute-atom SRO clusters in the α -Mg matrix. For the present Mg-Zn-Gd ternary alloys, it is anticipated that the T_V/T_H SRO clusters intrinsically accompany the Zn atoms, and hence we further examine the possible Zn positions that are energetically favored within the Gd trimmers.

Figure 5A shows the models placing a single Zn atom within the Gd trimer structures (T_V and T_H), and the formation energies calculated for each of the Zn positions are summarized in Figure 5B. For the both T_V and T_H , the Zn at the A sites appear to be the lowest formation energies with a significant energy gain about 398 and 447 meV/cell, respectively. Note that the Zn at the A sites show the energy differences larger than 100 meV/cell even compared with the next energetically-favored B sites, indicating that the Zn atoms at the A sites significantly stabilize the T_V/T_H structures. Hereafter, we denote these T_V/T_H SRO configurations of Zn/Gd atoms as a $D0_{19}$ -like $ZnGd_3$ cluster. It should be noted that the atomic positions in the $ZnGd_3$ cluster are relaxed from the ideal *hcp*-Mg structure; average Gd-Gd interatomic distances in the T_V - and T_H - $ZnGd_3$ clusters are estimated to be 4.40 and 4.46 Å, respectively, which are smaller than the relevant distance

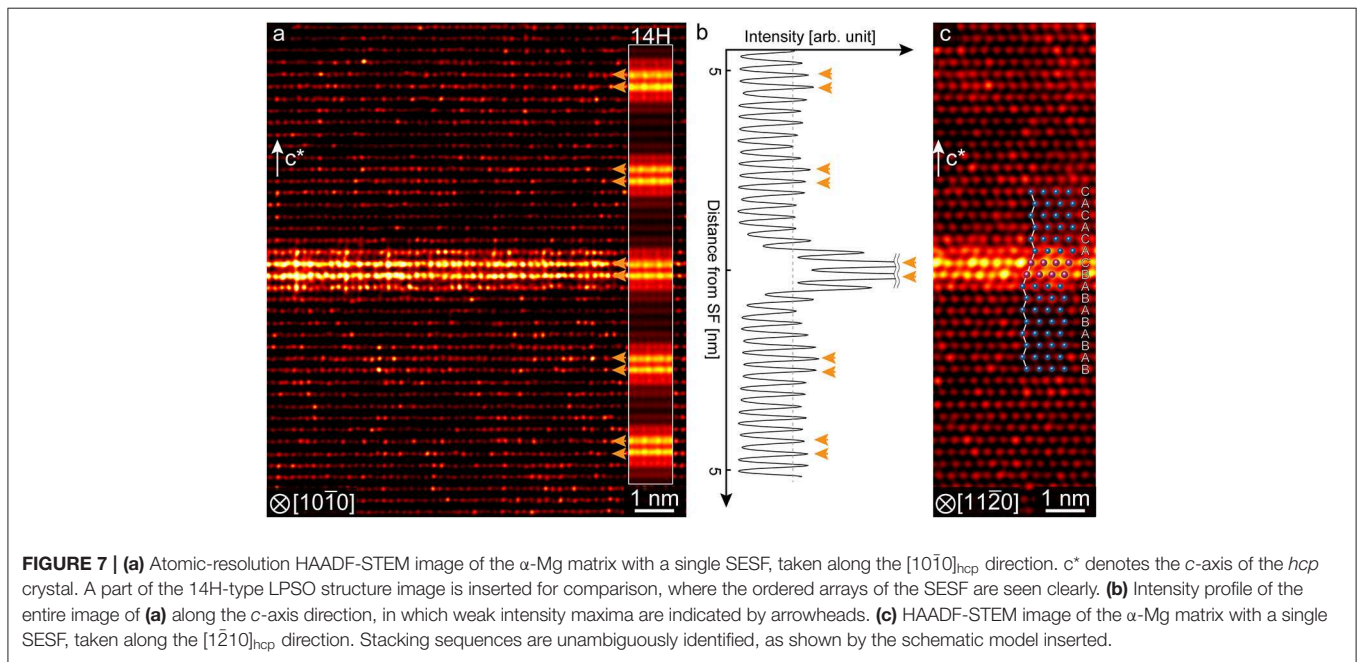
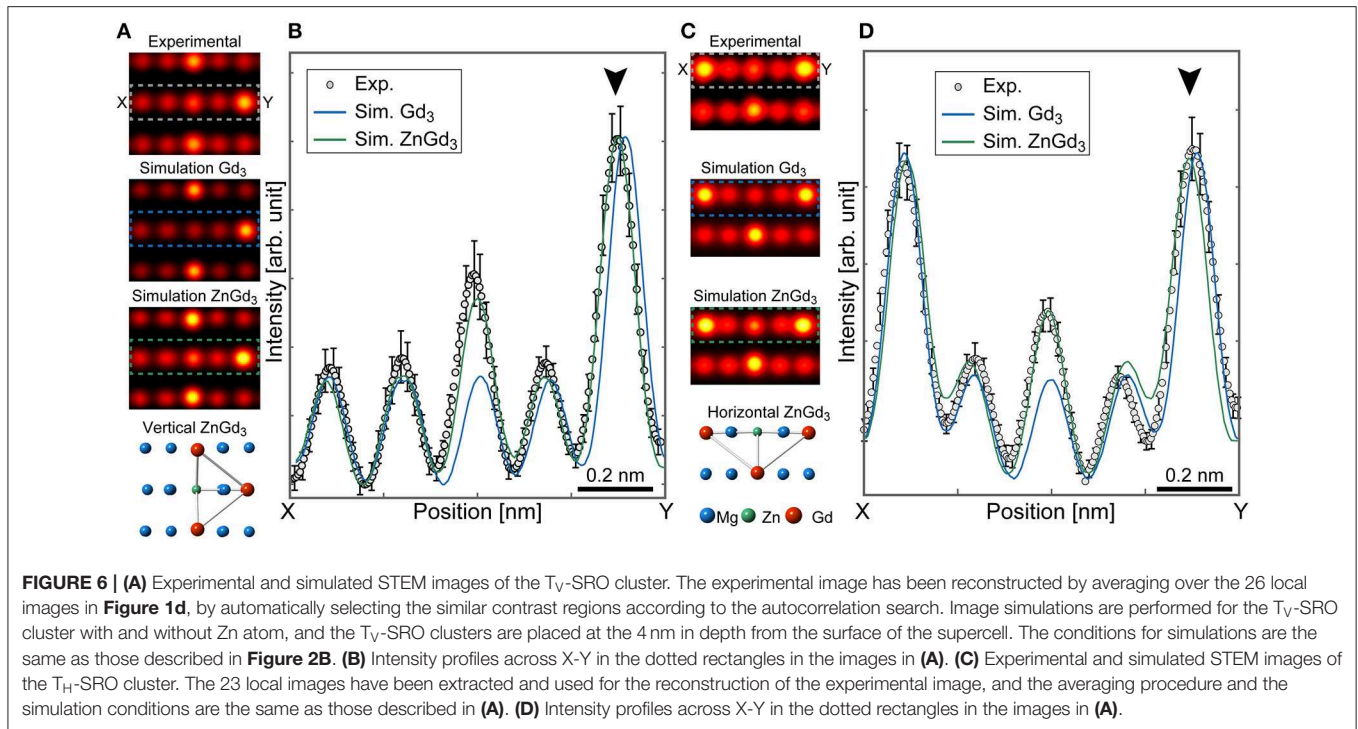


of 4.50 Å in the ideal *hcp*-Mg structure. It is worth mentioning here that, for the LPSO phase, the Gd-Gd interatomic distance in the $L1_2$ -type Zn_6Gd_8 cluster becomes 3.93 Å, being significantly shorter than that of the present $ZnGd_3$ clusters. This is perhaps originated from the strong condensations between the Zn/Gd atoms, causing significant relaxations whose displacements are likely to depend on a total number of the constituent solute atoms in the clusters.

The presence of the $D0_{19}$ -like $ZnGd_3$ clusters can be verified from the local intensity analysis of the HAADF-STEM images. **Figure 6A** shows the experimental and the simulated images of the T_V - $ZnGd_3$ SRO clusters. The experimental image is an averaged one that has been reconstructed by searching automatically the similar T_V -SRO contrast regions over the image (**Figure 3a**), according to the cross-correlation evaluation of the local contrast variations; e.g., as shown in **Figure 3a**, given yellow-square regions as the references, the similar contrast regions of white dashed squares have been selected (*template-matching*, see for details the supplement in Egami and Abe, 2015). Note that the T_V -SRO cluster has three variants and differently appear in the $\langle 1\bar{2}10 \rangle$ projections, and hence the extracted image of **Figure 6A** represents one of the variants. The image simulations are performed for the T_V - Gd_3 (**Figure 4D**) and the

T_V - $ZnGd_3$ (**Figure 5A**), whose intensity profiles are taken across the X-Y direction of each image and compared with that of the corresponding experiment image, as shown in **Figure 6B**. It is evident that the T_V -cluster with Zn provides significantly better fit to the observed intensity, confirming that the present T_V -SRO clusters are essentially a ternary $ZnGd_3$. We should also note that the slight peak-shift of the Gd position is also reproduced fairly well by the simulation with the Zn atom, as indicated by an arrowhead, supporting strongly the presence of the Zn atom that causes relaxation for the T_V - Gd_3 configurations and provides a considerable energy gain (**Figure 5B**). **Figures 6C,D** show a series of analysis for the T_H -type SRO cluster, as being made along with the same manner for the T_V -type SRO cluster described above. The experimental profiles are also reproduced significantly better by the simulation with the Zn-containing cluster, confirming that the T_H -type SRO cluster also forms as a ternary $ZnGd_3$.

Now that the SRO- $ZnGd_3$ clusters appear to be a $D0_{19}$ -like configuration, which prompts the notion about structural similarity with the $L1_2$ -type Zn_6Gd_8 cluster in the LPSO phase. In the both clusters, Gd atoms are placed at the second-nearest neighbor in the original *hcp*-Mg sites or the local *fcc* environment sites in the intrinsic-II type stacking fault (Egusa and Abe, 2012), and Zn occupies the first-nearest neighbor to these Gd atoms. This similarity in local structures supports an idea that the $D0_{19}$ -like $ZnGd_3$ cluster can be a precursor to the $L1_2$ -type Zn_6Gd_8 cluster, and the process must accompany the local *hcp-fcc* stacking change. With this in mind, we here focus on the spatial distribution of the $ZnGd_3$ clusters in the α -Mg matrix. **Figure 7a** shows an enlarged HAADF-STEM image of **Figure 1d** (green-rectangle region), where the single SESF is formed in the α -Mg matrix. A large number of bright spots clearly show up in the image, some of which indeed represent the $ZnGd_3$ clusters as described before. By carefully looking at the image, the bright spots seem to not distribute uniformly but form weak layered atmosphere. By tracing the entire intensity profile along the *c*-axis, as shown in **Figure 7b**, weak local maxima indeed appear at the positions indicated by arrowheads, these positions are at the distance from 7 or 14 atomic layers from the SESF, whose modulation length is equivalent to the *c*-axis correlation of the 14H-LPSO structure. As confirmed by the STEM image of the relevant region taken along the $[1\bar{2}10]$ direction (**Figure 7c**), there is no change in the stacking sequences except for the single SESF. Therefore, the observed intensity modulations imply that the $D0_{19}$ -like $ZnGd_3$ clusters form a layered solute atmosphere in the *hcp*-Mg matrix around the SESF, being prior to the introduction of stacking faults into the *hcp*-Mg matrix (similar phenomena was also reported for the Mg-Al-Gd system; Kishida et al., 2013). It should be noted here that the layered-atmosphere modulation across the *c*-axis is extended longer than a nanometer-scale, which may require long-range solute interactions significantly longer than those for the short-range clusters. At present, it is difficult to clarify the origin of such long-range correlations based on first-principle calculations with a limited number of solute atoms. The origin



might be interpreted by solute interactions with the multiple L_{12} -type clusters embedded within the SESF, the details of which will be described elsewhere.

CONCLUSION

In the present study, we have investigated the possible SRO clusters of solute Zn and Gd atoms formed in the annealed

$Mg_{97}Zn_1Gd_2$ alloy, based on aberration-corrected HAADF-STEM observations. The SRO structures have been successfully determined with the aid of STEM image simulations and first-principles calculations. The main results are summarized as follows.

1. HAADF-STEM imaging has confirmed presence of the solute-atom SRO clusters in the α -Mg phase as well as the LPSO phase. Quantitative image analyses with the aid of

simulations show that the observed intensity variations indeed reflect single Gd atom distributions. Characteristic SRO-related contrasts have been directly extracted from the image, emerging characteristic SRO configurations composed of three Gd atoms; vertical and horizontal trimers.

2. First-principles calculations have shown that the energetically-favored SRO configurations are the two types Gd trimer, which are represented as T_V - and T_H -SRO clusters and in good accordance with the STEM observations. Comprehensive investigations on possible Zn sites within the Gd-trimer clusters have shown that the Zn atoms are essentially involved both in the T_V - and T_H -SRO Gd clusters; $D0_{19}$ -like $ZnGd_3$ clusters have emerged as significantly energy-stabilized configurations.
3. It has been found that the $D0_{19}$ -like $ZnGd_3$ clusters seem to form weak layered-atmosphere around the isolated SESF. This may imply that, during the transformation from the *hcp*-Mg to the LPSO structure, the composition modulations along the *c*-axis take place prior to the introduction of the I_2 -SFs.

REFERENCES

- Abe, E., Kawamura, Y., Hayashi, K., and Inoue, A. (2002). Long-period ordered structure in a high-strength nanocrystalline Mg-1 at% Zn-2 at% Y alloy studied by atomic-resolution Z-contrast STEM. *Acta Mater.* 50, 3845–3857. doi: 10.1016/S1359-6454(02)00191-X
- Abe, E., Ono, A., Itoi, T., Yamasaki, M., and Kawamura, Y. (2011). Polytypes of long-period stacking structures synchronized with chemical order in a dilute Mg–Zn–Y alloy. *Philos. Magazine Lett.* 91, 690–696. doi: 10.1080/09500839.2011.609149
- Egami, M., and Abe, E. (2015). Structure of a novel Mg-rich complex compound in Mg–Co–Y ternary alloys. *Scripta Mater.* 98, 64–67. doi: 10.1016/j.scriptamat.2014.11.013
- Egusa, D., and Abe, E. (2012). The structure of long period stacking/order Mg–Zn–RE phases with extended non-stoichiometry ranges. *Acta Mater.* 60, 166–178. doi: 10.1016/j.actamat.2011.09.030
- Egusa, D., Yamasaki, M., Kawamura, Y., and Abe, E. (2013). Micro-kinking of the long-period stacking/order (LPSO) phase in a hot-extruded Mg₉₇Zn₁Y₂ alloy. *Mater. Transac.* 54, 698–702. doi: 10.2320/matertrans.MI201216
- Fujita, N., Matsushita, M., Tsukamoto, R., Yamasaki, M., Kawamura, Y., Irifune, T., et al. (2018). The structure of a novel long-period superlattice phase in Mg₉₇Zn₁Y₂ alloys. *Scripta Mater.* 150, 78–81. doi: 10.1016/j.scriptamat.2018.02.043
- Garcés, G., Máthis, K., Medina, J., Horváth, K., Drozdenko, D., Oñorbe, E., et al. (2018). Combination of *in-situ* diffraction experiments and acoustic emission testing to understand the compression behavior of Mg–Y–Zn alloys containing LPSO phase under different loading conditions. *Int. J. Plasticity* 106, 107–128. doi: 10.1016/j.ijplas.2018.03.004
- Gröbner, J., Kozlov, A., Fang, X.-Y., Zhu, S., Nie, J.-F., Gibson, M. A., et al. (2015). Phase equilibria and transformations in ternary Mg–Gd–Zn alloys. *Acta Mater.* 90, 400–416. doi: 10.1016/j.actamat.2015.02.044
- Gu, X.-F., Furuhashi, T., Chen, L., and Yang, P. (2018). Study on the planar segregation of solute atoms in Mg–Al–Gd alloy. *Scripta Mater.* 150, 45–49. doi: 10.1016/j.scriptamat.2018.02.041
- Hagihara, K., Kinoshita, A., Sugino, Y., Yamasaki, M., Kawamura, Y., Yasuda, H. Y., et al. (2010). Effect of long-period stacking ordered phase on mechanical properties of Mg₉₇Zn₁Y₂ extruded alloy. *Acta Mater.* 58, 6282–6293. doi: 10.1016/j.actamat.2010.07.050
- Hagihara, K., Li, Z., Yamasaki, M., Kawamura, Y., and Nakano, T. (2019). Strengthening mechanisms acting in extruded Mg-based long-period

DATA AVAILABILITY STATEMENT

All datasets generated for this study are included in the article/supplementary material.

AUTHOR CONTRIBUTIONS

EA initiated and designed the research and interpreted the data. DE and KK performed the experiments, analyzed the data, and carried out computer simulations. DE and EA wrote the paper.

FUNDING

This study was supported by JSPS KAKENHI for Scientific Research on Innovative Areas Materials Science of a Mille-feuille Structure (Grant Numbers JP18H05475, JP18H05479), and Nanotechnology Platform of the MEXT, Japan.

stacking ordered (LPSO)-phase alloys. *Acta Mater.* 163, 226–239. doi: 10.1016/j.actamat.2018.10.016

- He, S. M., Zeng, X. Q., Peng, L. M., Gao, X., Nie, J. F., and Ding, W. J. (2006). Precipitation in a Mg–10Gd–3Y–0.4Zr (wt.%) alloy during isothermal ageing at 250°C. *J. Alloys Compd.* 421, 309–313. doi: 10.1016/j.jallcom.2005.11.046
- Homma, T., Kunito, N., and Kamado, S. (2009). Fabrication of extraordinary high-strength magnesium alloy by hot extrusion. *Scripta Mater.* 61, 644–647. doi: 10.1016/j.scriptamat.2009.06.003
- Honma, T., Ohkubo, T., Hono, K., and Kamado, S. (2005). Chemistry of nanoscale precipitates in Mg–2.1Gd–0.6Y–0.2Zr (at.%) alloy investigated by the atom probe technique. *Mater. Sci. Eng. A* 395, 301–306. doi: 10.1016/j.msea.2004.12.035
- Honma, T., Ohkubo, T., Kamado, S., and Hono, K. (2007). Effect of Zn additions on the age-hardening of Mg–2.0Gd–1.2Y–0.2Zr alloys. *Acta Mater.* 55, 4137–4150. doi: 10.1016/j.actamat.2007.02.036
- Hosokawa, S., Stellhorn, J., Paulus, B., Maruyama, K., Kobayashi, K., Okuda, H., et al. (2018). The seeds of Zn₆Y₈ L1₂-type clusters in amorphous Mg₈₅Zn₆Y₉ alloy investigated by photoemission spectroscopy. *J. Alloy Compd.* 764, 431–436. doi: 10.1016/j.jallcom.2018.06.012
- Inamura, T. (2019). Geometry of kink microstructure analysed by rank-1 connection. *Acta Mater.* 173, 270–280. doi: 10.1016/j.actamat.2019.05.023
- Ishizuka, K. (2002). A practical approach for STEM image simulation based on the FFT multislice method. *Ultramicroscopy* 90, 71–83. doi: 10.1016/S0304-3991(01)00145-0
- Itoi, T., Seimiya, T., Kawamura, Y., and Hirohashi, M. (2004). Long period stacking structures observed in Mg₉₇Zn₁Y₂ alloy. *Scripta Mater.* 51, 107–111. doi: 10.1016/j.scriptamat.2004.04.003
- Jono, Y., Yamasaki, M., and Kawamura, Y. (2013). Effect of LPSO phase-stimulated texture evolution on creep resistance of extruded Mg–Zn–Gd alloys. *Mater. Transac.* 54, 703–712. doi: 10.2320/matertrans.MI201218
- Kawamura, Y., Hayashi, K., Inoue, A., and Masumoto, T. (2001). Rapidly solidified powder metallurgy Mg₉₇Zn₁Y₂ alloys with excellent tensile yield strength above 600 MPa. *Mater. Transac.* 42, 1172–1176. doi: 10.2320/matertrans.42.1172
- Kawamura, Y., and Yamasaki, M. (2007). Formation and mechanical properties of Mg₉₇Zn₁ RE₂ alloys with long-period stacking ordered structure. *Mater. Transac.* 48, 2986–2992. doi: 10.2320/matertrans.MER2007142
- Kim, J., and Kawamura, Y. (2013). Influence of rare earth elements on microstructure and mechanical properties of Mg₉₇Zn₁Y₁RE₁ alloys. *Mater. Sci. Eng.* 573, 62–66. doi: 10.1016/j.msea.2012.12.087

- Kimizuka, H., Kurokawa, S., Yamaguchi, A., Sakai, A., and Ogata, S. (2014). Two-dimensional ordering of solute nanoclusters at a close-packed stacking fault: modeling and experimental analysis. *Sci. Rep.* 4:7318. doi: 10.1038/srep07318
- Kishida, K., Yokobayashi, H., and Inui, H. (2013). The most stable crystal structure and the formation processes of an order-disorder (OD) intermetallic phase in the Mg–Al–Gd ternary system. *Philos. Magazine* 93, 2826–2846. doi: 10.1080/14786435.2013.790566
- Koizumi, T., Egami, M., Yamashita, K., and Abe, E. (2018). Platelet precipitate in an age-hardening Mg–Zn–Gd alloy. *J. Alloy Compd.* 752, 407–411. doi: 10.1016/j.jallcom.2018.04.136
- Kresse, G., and Furthmüller, J. (1996). Efficiency of ab-initio total energy calculations for metals and semiconductors using a plane-wave basis set. *Comput. Mater. Sci.* 6, 15–50. doi: 10.1016/0927-0256(96)00008-0
- Ma, S.-Y., Liu, L.-M., and Wang, S.-Q. (2013). The predominant role of Zn₆Y₉ cluster in the long period stacking order structures of Mg–Zn–Y alloys: a first-principles study. *J. Mater. Sci.* 48, 1407–1412. doi: 10.1007/s10853-012-6890-4
- Malis, T., Cheng, S., and Egerton, R. (1988). EELS log-ratio technique for specimen-thickness measurement in the TEM. *J. Electron. Microsc. Tech.* 8, 193–200. doi: 10.1002/jemt.1060080206
- Matsushita, M., Ingai, R., Yamasaki, M., Shinmei, T., Kawamura, Y., Irifune, T., et al. (2016). A novel long-period superlattice phase in Mg₉₇Zn₁Yb₂ alloys synthesized under high-pressure. *Scripta Mater.* 122, 45–49. doi: 10.1016/j.scriptamat.2016.04.022
- Mittal, A., and Mkhoyan, A. K. (2011). Limits in detecting an individual dopant atom embedded in a crystal. *Ultramicroscopy* 111, 1101–1110. doi: 10.1016/j.ultramic.2011.03.002
- Nie, J.-F. (2012). Precipitation and hardening in magnesium alloys. *Metal. Mater. Trans. A* 43, 3891–3939. doi: 10.1007/s11661-012-1217-2
- Nie, J. F., Oh-ishi, K., Gao, X., and Hono, K. (2008). Solute segregation and precipitation in a creep-resistant Mg–Gd–Zn alloy. *Acta Mater.* 56, 6061–6076. doi: 10.1016/j.actamat.2008.08.025
- Nishijima, M., and Hiraga, K. (2007). Structural changes of precipitates in an Mg–5 at%Gd alloy studied by transmission electron microscopy. *Mater. Trans.* 48, 10–15. doi: 10.2320/matertrans.48.10
- Nishijima, M., Hiraga, K., Yamasaki, M., and Kawamura, Y. (2008). The structure of guinier-preston zones in an Mg–2 at%Gd–1 at%Zn alloy studied by transmission electron microscopy. *Mater. Trans.* 49, 227–229. doi: 10.2320/matertrans.MEP2007257
- Nishioka, T., Yamamoto, Y., Kimura, K., Hagihara, K., Izuno, H., Hoppo, N., et al. (2018). In-plane positional correlations among dopants in 10H type long period stacking ordered Mg₇₅Zn₁₀Y₁₅ alloy studied by X-ray fluorescence holography. *Materialia* 3, 256–259. doi: 10.1016/j.mtla.2018.09.002
- Okuda, H., Yamasaki, M., and Kawamura, Y. (2017). Transition to long period stacking ordered structures in Mg₈₅Gd₉Zn₆ alloys from amorphous ribbons examined by synchrotron radiation scattering: comparison with Mg₈₅Y₉Zn₆ alloys. *Scripta Mater.* 139, 26–29. doi: 10.1016/j.scriptamat.2017.06.013
- Okuda, H., Yamasaki, M., Kawamura, Y., Tabuchi, M., and Kimizuka, H. (2015). Nanoclusters first: a hierarchical phase transformation in a novel Mg alloy. *Sci. Rep.* 5:14186. doi: 10.1038/srep14186
- Perdew, J., Chevary, J., Vosko, S., Jackson, K., Pederson, M., Singh, D., et al. (1992). Atoms, molecules, solids, and surfaces: applications of the generalized gradient approximation for exchange and correlation. *Phys. Rev. B* 46, 6671–6687. doi: 10.1103/PhysRevB.46.6671
- Pollock, T. M. (2010). Weight loss with magnesium alloys. *Science* 328, 986–987. doi: 10.1126/science.1182848
- Saal, J. E., and Wolverton, C. (2014). Thermodynamic stability of Mg-based ternary long-period stacking ordered structures. *Acta Mater.* 68, 325–338. doi: 10.1016/j.actamat.2013.10.055
- Saito, K., Yasuhara, A., and Hiraga, K. (2011). Microstructural changes of Guinier–Preston zones in an Mg–1.5at% Gd–1at% Zn alloy studied by HAADF-STEM technique. *J. Alloys Compd.* 509, 2031–2038. doi: 10.1016/j.jallcom.2010.10.129
- Sandlöbes, S., Pei, Z., Friák, M., Zhu, L.-F., Wang, F., Zaeferrer, S., et al. (2014). Ductility improvement of Mg alloys by solid solution: Ab initio modeling, synthesis and mechanical properties. *Acta Mater.* 70, 92–104. doi: 10.1016/j.actamat.2014.02.011
- Shao, X. H., Yang, Z. Q., and Ma, X. L. (2010). Strengthening and toughening mechanisms in Mg–Zn–Y alloy with a long period stacking ordered structure. *Acta Mater.* 58, 4760–4771. doi: 10.1016/j.actamat.2010.05.012
- Umehayashi, T., Iikubo, S., and Ohtani, H. (2014). Thermodynamic analysis on a segregation behavior of alloying elements to stacking faults in Mg–Y–Zn based LPSO structures. *J. Jpn. Inst. Metals Mater.* 78, 117–125. doi: 10.2320/jinstmet.JBW201307
- Xu, C., Zheng, M., Xu, S., Wu, K., Wang, E., Fan, G., et al. (2015). Improving strength and ductility of Mg–Gd–Y–Zn–Zr alloy simultaneously via extrusion, hot rolling and ageing. *Mater. Sci. Eng. A* 643, 137–141. doi: 10.1016/j.msea.2015.07.032
- Yamamoto, Y., Sakamoto, Y., Masaki, Y., and Nishitani, S. R. (2013). First principles calculations of solute ordering in Mg–Zn–Y alloys. *Mater. Trans.* 54, 656–660. doi: 10.2320/matertrans.MI201207
- Yamasaki, M., Anan, T., Yoshimoto, S., and Kawamura, Y. (2005). Mechanical properties of warm-extruded Mg–Zn–Gd alloy with coherent 14H long period stacking ordered structure precipitate. *Scripta Mater.* 53, 799–803. doi: 10.1016/j.scriptamat.2005.06.006
- Yamasaki, M., Hagihara, K., Inoue, S., Hadorn, J., and Kawamura, Y. (2013). Crystallographic classification of kink bands in an extruded Mg–Zn–Y alloy using intragranular misorientation axis analysis. *Acta Mater.* 61, 2065–2076. doi: 10.1016/j.actamat.2012.12.026
- Yamasaki, M., Matsushita, M., Hagihara, K., Izuno, H., Abe, E., and Kawamura, Y. (2014). Highly ordered 10H-type long-period stacking order phase in a Mg–Zn–Y ternary alloy. *Scripta Mater.* 78, 13–16. doi: 10.1016/j.scriptamat.2014.01.013
- Yamasaki, M., Sasaki, M., Nishijima, M., Hiraga, K., and Kawamura, Y. (2007). Formation of 14H long period stacking ordered structure and profuse stacking faults in Mg–Zn–Gd alloys during isothermal aging at high temperature. *Acta Mater.* 55, 6798–6805. doi: 10.1016/j.actamat.2007.08.033
- Yamashita, K., Itoi, T., Yamasaki, M., Kawamura, Y., and Abe, E. (2019). A novel long-period stacking/order structure in Mg–Ni–Y alloys. *J. Alloy Compd.* 788, 277–282. doi: 10.1016/j.jallcom.2019.02.219
- Yokobayashi, H., Kishida, K., Inui, H., Yamasaki, M., and Kawamura, Y. (2011). Enrichment of Gd and Al atoms in the quadruple close packed planes and their in-plane long-range ordering in the long period stacking-ordered phase in the Mg–Al–Gd system. *Acta Mater.* 59, 7287–7299. doi: 10.1016/j.actamat.2011.08.011
- Zhu, Y. M., Morton, A. J., and Nie, J. F. (2010). The 18R and 14H long-period stacking ordered structures in Mg–Y–Zn alloys. *Acta Mater.* 58, 2936–2947. doi: 10.1016/j.actamat.2010.01.022

Conflict of Interest: The authors declare that the research was conducted in the absence of any commercial or financial relationships that could be construed as a potential conflict of interest.

Copyright © 2019 Egusa, Kawaguchi and Abe. This is an open-access article distributed under the terms of the Creative Commons Attribution License (CC BY). The use, distribution or reproduction in other forums is permitted, provided the original author(s) and the copyright owner(s) are credited and that the original publication in this journal is cited, in accordance with accepted academic practice. No use, distribution or reproduction is permitted which does not comply with these terms.